

Non-Hermitian topological ohmmeter

Viktor Könye^{1,2,*}, Kyrylo Ochkan^{1,2,§}, Anastasiia Chyzhykova^{1,3}, Jan Carl Budich^{2,4,5},
Jeroen van den Brink^{1,2,6}, Ion Cosma Fulga^{1,2,†} and Joseph Dufouleur^{1,2,‡}

¹*IFW Dresden, Leibniz Institute for Solid State and Materials Research, Helmholtzstraße 20,
Dresden 01069, Germany*


²*Würzburg-Dresden Cluster of Excellence ct.qmat, Dresden 01062, Germany*

³*Taras Shevchenko National University of Kyiv, Volodymyrska Street 60, Kyiv 01033, Ukraine*

⁴*Institute of Theoretical Physics, Technische Universität Dresden, Dresden 01062, Germany*

⁵*Max Planck Institute for the Physics of Complex Systems, Nöthnitzer Str. 38, Dresden 01187, Germany*

⁶*Department of Physics, TU Dresden, Dresden 01062, Germany*

 (Received 6 October 2023; revised 28 March 2024; accepted 1 August 2024; published 3 September 2024)

Measuring large electrical resistances forms an essential part of common applications such as insulation testing but suffers from a fundamental problem: the larger the resistance, the less sensitive is a canonical ohmmeter. Here, we develop a conceptually different electronic sensor by exploiting the topological properties of non-Hermitian matrices, the eigenvalues of which can show an exponential sensitivity to perturbations. The ohmmeter is realized in a multiterminal linear electronic circuit with a non-Hermitian conductance matrix, where the target resistance plays the role of the perturbation. We inject multiple currents and measure a single voltage in order to directly obtain the value of the resistance. The relative accuracy of the device increases exponentially with the number of terminals and for large resistances outperforms a standard measurement by over an order of magnitude. Our work hopefully paves the way toward leveraging non-Hermitian conductance matrices in high-precision sensing.

DOI: [10.1103/PhysRevApplied.22.L031001](https://doi.org/10.1103/PhysRevApplied.22.L031001)

Small changes typically produce small effects. This common physical intuition has its roots in mathematics, where according to Weyl's inequality, the spectrum of a Hermitian matrix cannot change by an amount larger than the perturbation. Non-Hermitian matrices, however, are not constrained in this fashion. Instead, a small change can produce a large shift of the spectrum, in some cases even growing exponentially as a function of the matrix dimension. This counterintuitive property has recently been proposed as a way of constructing new sensor architectures [1–4]: In certain condensed-matter and optical systems, gain and loss may lead to an effectively non-Hermitian description of the wave-function dynamics, exhibiting enhanced sensitivity to small parameter changes. Specifically, an exponentially enhanced spectral sensitivity with respect to boundary conditions has been predicted [4] to occur as a consequence of nontrivial topology: it is protected by an integer-quantized winding number of the complex spectrum [5–8].

In parallel, it has been realized that signatures of nontrivial topology are not unique to condensed-matter

systems but can occur in a variety of other platforms, dubbed metamaterials [9–14]. Their dynamics mimics that of quantum wave functions evolving according to the Schrödinger equation, allowing for the experimental demonstration of different non-Hermitian topological phenomena [15–25].

Here, starting from these insights and with a focus on applications, we build a classical electronic circuit with a non-Hermitian topological conductance matrix [26,27] that functions as an ohmmeter. We consider a multiterminal system connected to a set of current sources and voltmeters that, in linear order, is described by a conductance matrix \hat{G} relating the current vector $\mathbf{I} = (I_1, \dots, I_N)$ to the voltage vector $\mathbf{V} = (V_1, \dots, V_N)$. We have used resistors and operational amplifiers connected in a voltage-follower configuration to build a circuit associated with a non-Hermitian conductance matrix, as shown in Fig. 1. The sensor circuit realizes an electronic counterpart of a non-Hermitian topological system investigated theoretically in the context of tight-binding models in Ref. [4] (see details of the model [4,28–32] in Sec. I of the Supplemental Material [33]). Here, the role of the Hermitian-coupling term between the first and the last sites of the tight-binding Hamiltonian is played by the resistor R in Fig. 1(b). In this work, we make use of the topological properties of the non-Hermitian \hat{G} matrix to measure the very large resistance R of the device under test (DUT) with enhanced precision.

*Contact author: konyeviktor@gmail.com

†Contact author: i.c.fulga@ifw-dresden.de

‡Contact author: j.dufouleur@ifw-dresden.de

§These two authors contributed equally to this work.

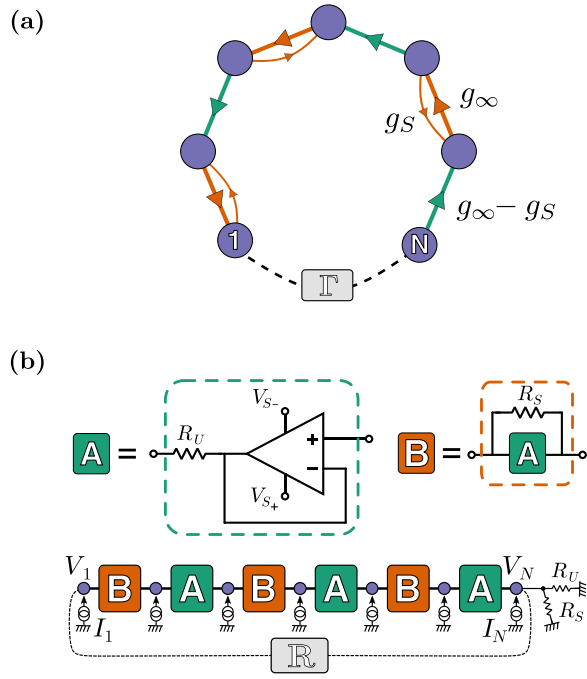


FIG. 1. The device schematics. (a) The structure of the conductance matrix given in Eq. (1) for seven terminals (purple circles), where g_S and g_∞ denote nonreciprocal couplings between adjacent terminals and Γ is the reciprocal coupling between the first and the last terminal. (b) The electronic-circuit realization using operational amplifiers and resistances, where the coupling between the two end terminals is realized by the resistance $R = -1/\Gamma$.

A standard method to measure large resistances is the constant-voltage method, where a known (large) voltage is sourced and the current flowing through the DUT is measured. The resistance is given by the ratio between the voltage applied on the DUT and the current, the latter usually being determined by measuring the voltage drop on a well-calibrated test resistance. Such a current vanishes as the resistance R of the DUT increases and high-precision measurements of infinitesimal currents are required to achieve a decent measurement of resistances above the mega-ohm regime. The precision of the current measurement sets the precision of the resistance measurement, which decreases continuously when R increases. Unlike the standard method, we consider here a multiple-source device the sensitivity of which increases exponentially with the number of terminals.

The conductance matrix of the electronic circuit in Fig. 1 (for five terminals) is of the form

$$\hat{G} = \begin{pmatrix} g_\infty - \Gamma & -g_S & 0 & 0 & \Gamma \\ -g_S & g_\infty & -g_\infty + g_S & 0 & 0 \\ 0 & 0 & g_\infty & -g_\infty & 0 \\ 0 & 0 & -g_S & g_\infty & -g_\infty + g_S \\ \Gamma & 0 & 0 & 0 & g_\infty - \Gamma \end{pmatrix}, \quad (1)$$

where $g_\infty = 1/R_U + 1/R_S$, $\Gamma = -1/R$, and $g_S = 1/R_S$. R_U is the unidirectional resistance associated with the voltage follower, R_S is a resistance that appears between adjacent terminals in a staggered way, and R is the resistance of the DUT, which connects the first terminal to the last one in our electronic circuit, controlling the boundary condition. Since we are interested in measuring small variations in the large R value, we consider the regime in which $R \gg R_S, R_U$, so that the resistance is only perturbatively connecting the first terminal to the last one. The difference between Eq. (1) and the tight-binding Hamiltonian matrix considered in Ref. [4] is the $-\Gamma$ at the two ends of the main diagonal (for more information on the non-Hermitian tight-binding model, see Sec. I of the Supplemental Material [33]).

We consider the $\hat{G}\mathbf{V}_r = g(R)\mathbf{V}_r$ right-eigenvalue problem, where the \mathbf{V}_r are the right-voltage eigenvectors of the conductance matrix and g is the corresponding eigenvalue (for non-Hermitian matrices, the left and right eigenvectors are not equivalent—for mathematical details, see, e.g., Ref. [34]). Taking the $R \rightarrow \infty$ ($\Gamma = 0$) limit, we obtain the open boundary conditions of the non-Hermitian matrix. In this case, for any odd number of terminals, the matrix is guaranteed to have an eigenvalue equal to $g_0(\infty) = 1/R_S + 1/R_U \equiv g_\infty$. In the language of condensed-matter physics, this property is protected by the sublattice symmetry [4] (see Sec. I of the Supplemental Material [33]). We focus on the g_∞ eigenvalue below.

For finite resistance R , the shift of $g_0(R)$ is given by $\Delta g_0(R) = g_0(R) - g_\infty$ [see Figs. 2(a)–2(c)]. For large enough R , the modulus of $g_0(R)$ is well separated from the modulus of any other eigenvalue [see Fig. 2(a)]. We call this the perturbative, or “separated eigenvalues,” regime. Going to smaller R , this no longer holds: as shown in Figs. 2(a) and 2(b), $g_0(R)$ merges with another eigenvalue as R is decreased. The pair of eigenvalues then acquire nonzero imaginary parts and have equal absolute values. More details on the eigenvalues as a function of R are given in Sec. II of the Supplemental Material [33].

At large enough resistances, where the $g_0(R)$ eigenvalue is well separated, we can use perturbation theory [4] to track the evolution of Δg_0 (for details, see Sec. I of the Supplemental Material [33]):

$$\begin{aligned} \Delta g_0(R) &\approx \frac{\mathbf{V}_{1\infty}^\dagger \hat{G} \mathbf{V}_{r\infty}}{\mathbf{V}_{1\infty}^\dagger \mathbf{V}_{r\infty}} - g_\infty \\ &= \left[\left(-\frac{R_S}{R_U} \right)^{\frac{N-1}{2}} - 1 \right] \frac{1}{R}. \end{aligned} \quad (2)$$

Here, $\mathbf{V}_{1\infty}$ and $\mathbf{V}_{r\infty}$ are the left and right eigenvectors of \hat{G} at $R \rightarrow \infty$ and N is the number of terminals. We also calculate the change Δg_0 as a function of $1/R$ numerically from \hat{G} , as shown in Fig. 2(c) by the solid and dashed

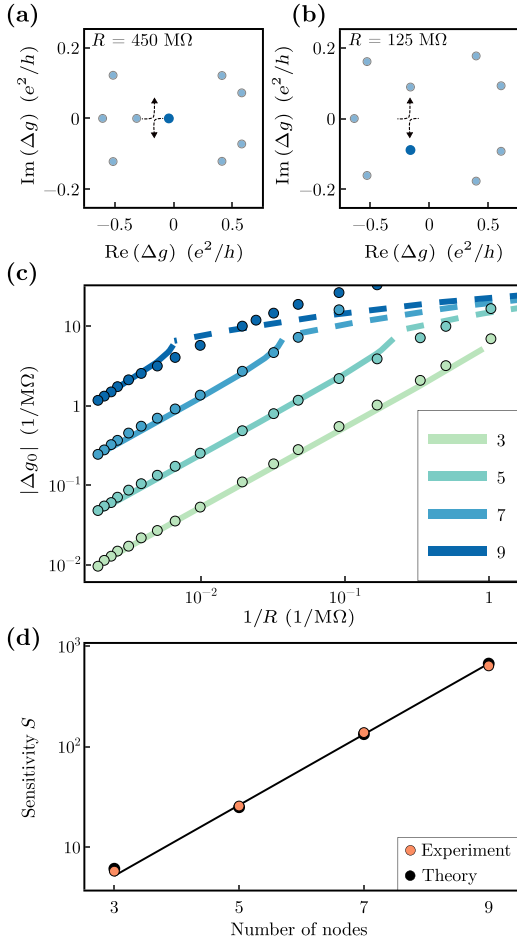


FIG. 2. The eigenvalue shift and sensitivity of the device. (a) Eigenspectra of an ideal nine-terminal conductance matrix for the case of separated and (b) unseparated eigenvalues. For each eigenvalue g_n of \hat{G} , $\Delta g = g_n - g_\infty$. The highlighted eigenvalue corresponds to Δg_0 . The dashed arrows indicate how the eigenvalues evolve as R is decreased. (c) The predicted shift in the conductance eigenvalue g_0 as a function of $1/R$ (lines) compared with the experimental data (points) for different numbers of terminals. The solid and dashed lines correspond to the region of separated and unseparated eigenvalues, respectively. (d) The predicted sensitivity [see Eq. (3)] for different numbers of terminals compared to the experimental values calculated with Eq. (6), using data presented in (c). Only the points that correspond to the perturbative regime (separated eigenvalues) have been used. The error bar is smaller than the symbol size.

lines, with the solid lines showing where the perturbative results are valid. The figure shows that for more terminals, the resistances at which the perturbative results hold become larger. Recently, we have become aware that such a shift of the eigenvalues has been measured in optics [35] and has been used to measure capacitances in electronic circuits [36].

Using the definition of Ref. [4] for the sensitivity S as the change of the eigenvalue with respect to the change in the

boundary conditions (for the definition and main properties of S as well as K and ε defined below, see also Sec. III of the Supplemental Material [33]), we obtain

$$S = \frac{dg_0}{d(1/R)} = \left(-\frac{R_S}{R_U} \right)^{\frac{N-1}{2}} - 1. \quad (3)$$

The expected perturbative values for the sensitivity are shown in Fig. 2(d). In practice, R_S and R_U may take a large range of values and could be optimized such as to produce a maximal sensitivity to the target resistance R . Importantly, the system shows exponential sensitivity when the non-Hermitian topological invariant (non-Hermitian winding number) is nontrivial. Because of this topological protection, the exponential sensitivity persists even with disorder in the matrix elements. For a proof of principle, we take here $R_S = 130 \text{ k}\Omega$ and $R_U = 25.5 \text{ k}\Omega$.

We connect the first and the last terminals with a resistance R and inject the $\mathbf{I}_{r\infty} \propto \mathbf{V}_{r\infty}$ current eigenvector into the device (see Sec. I of the Supplemental Material [33]). Note that this means that multiple current sources are used simultaneously. Each of the currents is generated by applying a low-frequency ac voltage on a $1\text{-M}\Omega$ resistor with the source of a SR 830 lock-in amplifier. The voltages are measured with the same lock-in amplifiers, with an input impedance of about $10 \text{ M}\Omega$. The measurements are carried out at low frequency ($f = 132.82 \text{ Hz}$). We use AD 823A FET input operational amplifiers for building the electronic circuit. In the case of three, five, seven, and nine terminals, the current vectors (see Sec. I of the Supplemental Material [33]) used in the experiment are

$$\mathbf{I}_3 = \begin{pmatrix} 4816 \\ 0 \\ -942 \end{pmatrix} \text{ nA}, \quad \mathbf{I}_5 = \begin{pmatrix} 5000 \\ 0 \\ -981 \\ 0 \\ 192 \end{pmatrix} \text{ nA},$$

$$\mathbf{I}_7 = \begin{pmatrix} 4240 \\ 0 \\ -832 \\ 0 \\ 162 \\ 0 \\ -32 \end{pmatrix} \text{ nA}, \quad \mathbf{I}_9 = \begin{pmatrix} 4050 \\ 0 \\ -794 \\ 0 \\ 156 \\ 0 \\ -31 \\ 0 \\ 6 \end{pmatrix} \text{ nA}. \quad (4)$$

Measuring the voltage V_N on the last terminal and dividing by the current on the last terminal I_N enables us to experimentally determine the eigenvalue shift, since (for details, see Sec. I of the Supplemental Material [33])

$$\frac{V_N}{I_N} \approx \frac{1}{g_0(R)} = \frac{1}{\frac{S}{R} + g_\infty}. \quad (5)$$

The measured values for $\Delta g_0(R)$ are shown in Fig. 2(c), together with the theoretical prediction. The value of g_∞ is determined separately for each point by measuring V_N without connecting the resistance R prior to any finite R measurement, in order to get rid of slow drifts of the voltages, and each data point corresponds to an average over 30 measurements (for details, see Sec. IV of the Supplemental Material [33]). There is a very good agreement between the experimental data and the exact eigenvalues for large R values, where the perturbative results hold.

Using the measured value for the voltage and the value for the injected current, we can also estimate S as

$$S = R \left(\frac{I_N}{V_N} - g_\infty \right). \quad (6)$$

We calculate the experimental value of S using this formula for resistances in the range of validity of the perturbative theory [based on the solid lines of Fig. 2(c)]. The results are shown in Fig. 2(d) and they are in good agreement with the theoretical predictions.

For small changes ΔR of the large target resistance, the sensor gives an Ohmic relationship between ΔR and the change in voltage ΔV_N : $\Delta V_N \propto \Delta R$. We therefore define the dimensionless relative slope K as

$$K = \frac{dV_N}{dR} \frac{R}{V_N}. \quad (7)$$

K is independent of the input current I_1 and can be expressed as (for details, see Sec. I of the Supplemental Material [33])

$$K \approx \frac{I_1}{(S/R + g_\infty)^2 R V_N} = \frac{\frac{S}{R}}{\frac{S}{R} + g_\infty}. \quad (8)$$

K characterizes the relative accuracy of our device. The resistance noise-to-signal ratio $\varepsilon_R = \Delta R/R$, where ΔR is the resistance noise (the absolute precision of the device) associated with the voltage noise measured, ΔV , depends on the voltage noise-to-signal ratio $\varepsilon_V = \Delta V/V$ (see Sec. III of the Supplemental Material [33]) as follows:

$$\varepsilon_R = \frac{\varepsilon_V}{K}. \quad (9)$$

A larger K thus improves the accuracy of the device. From Eq. (8), we can see that $K < 1$ always holds and from Eq. (3) we can see that K grows monotonically as a function of the number of terminals, N . This means that for a given resistance, the accuracy can be improved by increasing the number of nodes, provided that the perturbation theory results hold. If the current vector is large enough, the exponential increase in K is accompanied by an exponential increase in the signal-to-noise ratio $1/\varepsilon_R$

that corresponds to the precision of the sensor (see Secs. V and VI of the Supplemental Material [33]). We note that since we have set the system in the separated-eigenvalues regime, we are far from an exceptional point and we avoid any noise increase related to such specific operating points [37].

The theoretical values for K and the experimentally obtained values are shown in Fig. 3(a) as a function of the number of terminals N , for which the perturbative theory holds, and for two different test resistances (50 M Ω and 250 M Ω). The measurement procedure is described in detail in Sec. V of the Supplemental Material [33].

In order to compare the performance of the non-Hermitian ohmmeter with a standard measurement, we measure the resistance R with the circuit shown in the inset of Fig. 3(b), corresponding to the simplest configuration of a standard single-terminal circuit. We use the same lock-in amplifiers for sourcing and measuring

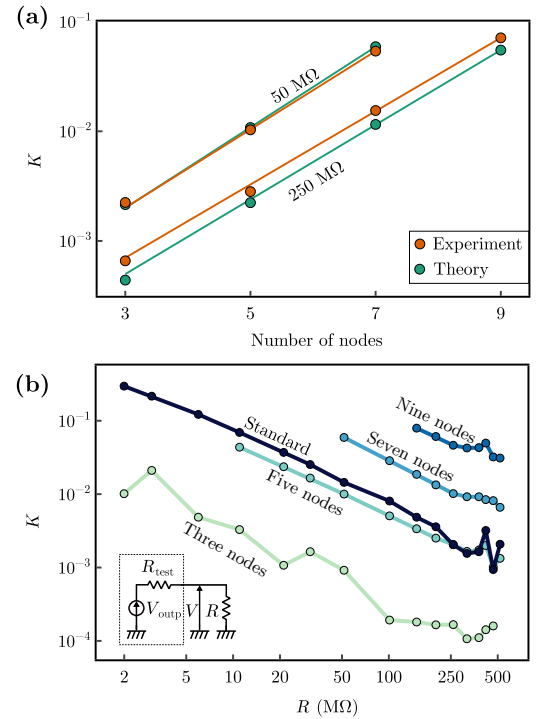


FIG. 3. The relative slope K . (a) The relative slope versus different numbers of nodes for $R \sim 50$ M Ω and for $R \sim 250$ M Ω . The measurements are realized over a range of resistance values corresponding to 10% of R (see Sec. V of the Supplemental Material [33]). The theoretical points correspond to the perturbation theory expectation given in Eq. (8). The solid lines correspond to linear fits. (b) A comparison between the K values for a standard single-terminal measurement and for sensors with different numbers of terminals. The data points for the sensors are obtained in the same way as in (a). The inset shows a standard single-terminal measurement electronic schematic, where the dashed line identifies the single-terminal ohmmeter device with $R_{\text{test}} = 1$ M Ω and $V_{\text{output}} = 1$ V.

as for the non-Hermitian ohmmeter. In this circuit, the well-calibrated resistance R_{test} allows us to determine the current flowing through the resistance R of the DUT, $I = (V_{\text{outp}} - V)/R_{\text{test}}$, leading to the trivial voltage-divider relation between the measured voltage V and the resistance to be measured, R : $V = V_{\text{outp}}R/(R + R_{\text{test}})$. In the constant-voltage mode, R_{test} should be as large as possible to maximize the accuracy of the measurement but it should remain much smaller than the resistance R in parallel with the input resistance of the lock-in amplifier ($R_{\text{lock}} \sim 10 \text{ M}\Omega$) to ensure a constant voltage drop on R . We choose $R_{\text{test}} = 1 \text{ M}\Omega$, a value that fulfills these two conditions and that corresponds to the polarization resistance used for the non-Hermitian ohmmeter. The results are shown in Fig. 3(b). The parameter K shows the same trend as a function of R for all measurements but can be exponentially increased for a larger number of terminals of the non-Hermitian device. Thus, we observe that the relative accuracy of the non-Hermitian ohmmeter outperforms that of the simple single-terminal measurement starting at $N = 7$ and becomes one order of magnitude larger at $N = 9$.

Note added. We note that, in parallel to our work, such a shift of the eigenvalues was recently measured in optics [35] and has been used to measure capacitances in electronic circuits [36].

The data and codes used in this work are available on Zenodo [38].

Acknowledgments. This work was supported by the Deutsche Forschungsgemeinschaft (DFG, German Research Foundation) under Germany's Excellence Strategy through the Würzburg-Dresden Cluster of Excellence on Complexity and Topology in Quantum Matter—*ct.qmat* (EXC 2147, project IDs 390858490, 242021 and 252023). J.C.B. acknowledges financial support via the DFG Project No. 459864239.

I.C.F. and J.C.B. conceived the theoretical framework of the project; I.C.F., J.v.d.B., and J.D. supervised the project. K.O., A.C., and J.D. designed the circuit, conducted the measurements, and analyzed the data. V.K. performed the analytical calculations and numerical simulations, using the idealized and measured conductance matrices to test the feasibility of the device, with inputs from J.C.B., J.v.d.B., and I.C.F. All authors participated in interpreting the results and writing the manuscript.

-
- [1] J. Wiersig, Enhancing the sensitivity of frequency and energy splitting detection by using exceptional points: Application to microcavity sensors for single-particle detection, *Phys. Rev. Lett.* **112**, 203901 (2014).
 [2] H. Hodaie, A. U. Hassan, S. Wittek, H. Garcia-Gracia, R. El-Ganainy, D. N. Christodoulides, and M. Khajavikhan,

- Enhanced sensitivity at higher-order exceptional points, *Nature* **548**, 187 (2017).
 [3] W. Chen, Ş. K. Özdemir, G. Zhao, J. Wiersig, and L. Yang, Exceptional points enhance sensing in an optical microcavity, *Nature* **548**, 192 (2017).
 [4] J. C. Budich and E. J. Bergholtz, Non-Hermitian topological sensors, *Phys. Rev. Lett.* **125**, 00 (2020).
 [5] Z. Gong, Y. Ashida, K. Kawabata, K. Takasan, S. Higashikawa, and M. Ueda, Topological phases of non-Hermitian systems, *Phys. Rev. X* **8**, 031079 (2018).
 [6] D. S. Borgnia, A. J. Kruchkov, and R. J. Slager, Non-Hermitian boundary modes and topology, *Phys. Rev. Lett.* **124**, 056802 (2020).
 [7] N. Okuma, K. Kawabata, K. Shiozaki, and M. Sato, Topological origin of non-Hermitian skin effects, *Phys. Rev. Lett.* **124**, 086801 (2020).
 [8] E. J. Bergholtz, J. C. Budich, and F. K. Kunst, Exceptional topology of non-Hermitian systems, *Rev. Mod. Phys.* **93**, 015005 (2021).
 [9] L. Lu, J. D. Joannopoulos, and M. Soljačić, Topological photonics, *Nat. Photonics* **8**, 821 (2014).
 [10] V. V. Albert, L. I. Glazman, and L. Jiang, Topological properties of linear circuit lattices, *Phys. Rev. Lett.* **114**, 173902 (2015).
 [11] Z. Yang, F. Gao, X. Shi, X. Lin, Z. Gao, Y. Chong, and B. Zhang, Topological acoustics, *Phys. Rev. Lett.* **114**, 114301 (2015).
 [12] R. Süssstrunk and S. D. Huber, Observation of phononic helical edge states in a mechanical topological insulator, *Science* **349**, 47 (2015).
 [13] W. Hu, J. C. Pillay, K. Wu, M. Pasek, P. P. Shum, and Y. Chong, Measurement of a topological edge invariant in a microwave network, *Phys. Rev. X* **5**, 011012 (2015).
 [14] N. Goldman, J. C. Budich, and P. Zoller, Topological quantum matter with ultracold gases in optical lattices, *Nat. Phys.* **12**, 639 (2016).
 [15] M. Brandenbourger, X. Locsin, E. Lerner, and C. Coullais, Non-reciprocal robotic metamaterials, *Nat. Commun.* **10**, 1 (2019).
 [16] C. H. Lee and R. Thomale, Anatomy of skin modes and topology in non-Hermitian systems, *Phys. Rev. B* **99**, 201103(R) (2019).
 [17] A. Ghatak, M. Brandenbourger, J. Van Wezel, and C. Coullais, Observation of non-Hermitian topology and its bulk-edge correspondence in an active mechanical metamaterial, *Proc. Natl. Acad. Sci. USA* **117**, 29561 (2020).
 [18] S. Weidemann, M. Kremer, T. Helbig, T. Hofmann, A. Stegmaier, M. Greiter, R. Thomale, and A. Szameit, Topological funneling of light, *Science* **368**, 311 (2020).
 [19] T. Helbig, T. Hofmann, S. Imhof, M. Abdelghany, T. Kiessling, L. W. Molenkamp, C. H. Lee, A. Szameit, M. Greiter, and R. Thomale, Generalized bulk-boundary correspondence in non-Hermitian topoelectrical circuits, *Nat. Phys.* **16**, 747 (2020).
 [20] L. Xiao, T. Deng, K. Wang, G. Zhu, Z. Wang, W. Yi, and P. Xue, Non-Hermitian bulk-boundary correspondence in quantum dynamics, *Nat. Phys.* **16**, 761 (2020).

- [21] X. Zhang, Y. Tian, J. H. Jiang, M. H. Lu, and Y. F. Chen, Observation of higher-order non-Hermitian skin effect, *Nat. Commun.* **12**, 1 (2021).
- [22] L. Zhang, Y. Yang, Y. Ge, Y. J. Guan, Q. Chen, Q. Yan, F. Chen, R. Xi, Y. Li, D. Jia, S. Q. Yuan, H. X. Sun, H. Chen, and B. Zhang, Acoustic non-Hermitian skin effect from twisted winding topology, *Nat. Commun.* **12**, 1 (2021).
- [23] H. Wang, X. Zhang, J. Hua, D. Lei, M. Lu, and Y. Chen, Topological physics of non-Hermitian optics and photonics: A review, *J. Opt.* **23**, 123001 (2021).
- [24] S. Liu, R. Shao, S. Ma, L. Zhang, O. You, H. Wu, Y. J. Xiang, T. J. Cui, and S. Zhang, Non-Hermitian skin effect in a non-Hermitian electrical circuit, *Research* **2021**, 1 (2021).
- [25] Q. Liang, D. Xie, Z. Dong, H. Li, H. Li, B. Gadway, W. Yi, and B. Yan, Dynamic signatures of non-Hermitian skin effect and topology in ultracold atoms, *Phys. Rev. Lett.* **129**, 070401 (2022).
- [26] S. Franca, V. Könye, F. Hassler, J. van den Brink, and C. Fulga, Non-Hermitian physics without gain or loss: The skin effect of reflected waves, *Phys. Rev. Lett.* **129**, 086601 (2022).
- [27] K. Ochkan, R. Chaturvedi, V. Könye, L. Veyrat, R. Giraud, D. Mailly, A. Cavanna, U. Gennser, E. M. Hankiewicz, B. Büchner, J. van den Brink, J. Dufouleur, and I. C. Fulga, Non-Hermitian topology in a multi-terminal quantum Hall device, *Nat. Phys.* **20**, 395 (2024).
- [28] S. Lieu, Topological phases in the non-Hermitian Su-Schrieffer-Heeger model, *Phys. Rev. B* **97**, 045106 (2018).
- [29] W. P. W. Su, J. R. Schrieffer, and A. J. Heeger, Solitons in polyacetylene, *Phys. Rev. Lett.* **42**, 1698 (1979).
- [30] N. Hatano and D. R. Nelson, Localization transitions in non-Hermitian quantum mechanics, *Phys. Rev. Lett.* **77**, 570 (1996).
- [31] F. K. Kunst, M. Trescher, and E. J. Bergholtz, Anatomy of topological surface states: Exact solutions from destructive interference on frustrated lattices, *Phys. Rev. B* **96**, 085443 (2017).
- [32] F. K. Kunst, E. Edvardsson, J. C. Budich, and E. J. Bergholtz, Biorthogonal bulk-boundary correspondence in non-Hermitian systems, *Phys. Rev. Lett.* **121**, 026808 (2018).
- [33] See the Supplemental Material at <http://link.aps.org/supplemental/10.1103/PhysRevApplied.22.L031001> for more details on the perturbative results, the conductance-matrix eigenspectra, fluctuations and signal-to-noise-ratio analysis, and measurement details.
- [34] Y. Ashida, Z. Gong, and M. Ueda, Non-Hermitian physics, *Adv. Phys.* **69**, 249 (2020).
- [35] M. Parto, C. Leefmans, J. Williams, and A. Marandi, Enhanced sensitivity via non-Hermitian topology, *ArXiv: 2305.03282*.
- [36] H. Yuan, W. Zhang, Z. Zhou, W. Wang, N. Pan, Y. Feng, H. Sun, and X. Zhang, Non-Hermitian topoelectrical circuit sensor with high sensitivity, *Adv. Sci.* **10**, 2301128 (2023).
- [37] H. Wang, Y.-H. Lai, Z. Yuan, M.-G. Suh, and K. Vahala, Petermann-factor sensitivity limit near an exceptional point in a Brillouin ring laser gyroscope, *Nat. Commun.* **11**, 1610 (2020).
- [38] V. Könye, K. Ochkan, A. Chyzykova, J. C. Budich, J. van den Brink, I. C. Fulga, and J. Dufouleur, Non-Hermitian topological ohmmeter, Zenodo (2023).